Complex rupture evolution of the 2007 Martinique earthquake: a non-double-couple event in the Caribbean Sea

Kenta Ohara[1], Yuji Yagi[2] and Ryo Okuwaki[2,3]

[1]Graduate School of Science and Technology, University of Tsukuba, Tsukuba, Ibaraki 305-8572, Japan.

[2]Faculty of Life and Environmental Sciences, University of Tsukuba, Tsukuba, Ibaraki 305-8572, Japan.

[3]Mountain Science Center, University of Tsukuba, Tsukuba, Ibaraki 305-8572, Japan.

Corresponding author: Kenta Ohara (kohrseismo@gmail.com)

Abbreviated title for page headings: Complex rupture of the 2007 Martinique earthquake

Summary

A large non-double-couple component of a tectonic earthquake indicates that its rupture likely was complex and likely involved multiple faults. Detailed source models of such earthquakes can add to our understanding of earthquake source complexity. The 2007 Martinique earthquake in the Caribbean Sea is one of the largest recent earthquakes with a known large non-double-couple component. It was an intermediate depth intraslab earthquake within the South America plate where it is subducting beneath the Caribbean plate. We applied potency density tensor inversion (PDTI) to teleseismic *P* waves generated by the 2007 Martinique earthquake to model its source processes and focal mechanism distribution. We identified two focal mechanisms: a strike-slip mechanism with a north–south T axis, and a down-dip extension (DDE) mechanism with an east–west T axis. Rupture by the DDE mechanism was predominant in the northern part of the source region and strike-slip rupture in the southern part. These two focal mechanisms had approximately parallel P axes and approximately orthogonal T axes. The seismic moments released by both types of rupture were almost equal. These results indicate that the 2007 Martinique earthquake had a large non-double-couple component. We identified five sub-events with two predominant directions of rupture propagation: two strike-slip sub-events propagated to the southeast and three DDE sub-events propagated to the east.

Although the directions of propagation were consistent for each focal mechanism, each sub-event appears to have occurred in isolation. For example, the rupture of one DDE sub-event propagated from the edge of the source region back towards the hypocentre. Complex ruptures that include multiple sub-events may be influenced by high pore fluid pressure associated with slab dehydration. Our results show that PDTI can produce stable estimates of complex seismic source processes and provide useful information about the sources of complex intermediate depth intraslab earthquakes for which fault geometry assumptions are difficult.

Key words: Inverse theory; Waveform inversion; Body waves; Earthquake dynamics; Earthquake source observations.

INTRODUCTION

Fault geometry provides important information about the controls on an earthquake's rupture evolution; for example, a complex fault geometry often leads to a complex rupture evolution (e.g. Meng *et al*. 2012; Yue *et al*. 2012; Avouac *et al*. 2014; Xu *et al*. 2018). Earthquake fault geometry or its complexity can be accessed through moment tensor solutions. For example, the Global Centroid Moment Tensor (GCMT) project (Dziewonski *et al.* 1981; Ekström *et al.* 2012) has determined moment tensor solutions for moderate-to-great earthquakes that are useful for interpreting earthquake source information such as fault geometry. Moment tensor solutions with components that cannot be explained by a double-couple source alone may indicate the presence of multiple or complex faults (e.g. Frohlich *et al*. 1989; Kuge & Kawakatsu 1993; Kuge & Lay 1994; Abercrombie *et al*. 2003).

The proportion of the non-double-couple component of an earthquake can be quantified by the relationship

$$\varepsilon = -\lambda_2 / \max(|\lambda_1|, |\lambda_3|), \quad (1)$$

where λ_i is the *i*th eigenvalue of a moment tensor ($\lambda_1 \geq \lambda_2 \geq \lambda_3$) (e.g. Dziewonski *et al*. 1981; Kuge & Kawakatsu 1990). For a double-couple moment tensor, $\varepsilon = 0$, whereas

for a compensated linear vector dipole moment tensor $|\varepsilon| = 0.5$ (Knopoff & Randall 1970). The proportion of the non-double-couple component is calculated as $|\varepsilon| \times 200$.

Among the GCMT solutions for 15,665 earthquakes of moment magnitude M_w > 5.5 (Dziewonski *et al.* 1981; Ekström *et al.* 2012), those with a >85% non-double-couple (NDC) proportion represent only 0.4% of the events between January 1976 and February 2023 (Fig. 1). The 2007 Martinique earthquake (M_w 7.4, 90% NDC component) is among the largest of the earthquakes with large NDC components (>85%; Fig. 1). Its epicentre lies between the islands of Dominica and Martinique in the Lesser Antilles island arc (United States Geological Survey; USGS 2007), where the South America plate is subducting westwards to south-westwards beneath the Caribbean plate (Sykes *et al.* 1982; DeMets *et al.* 2010; Cooper *et al.* 2020) (Fig. 2). The hypocentral depth of the 2007 earthquake was 156 km (USGS 2007), deeper than the top of the subducting plate (Hayes *et al.* 2018), thus indicating that the 2007 Martinique earthquake was an intermediate depth intraslab earthquake (Fig. 2). The GCMT solution shows the P axis azimuth is east-northeast and plunges eastwards at about 45°, and the T axis azimuth is northwest with almost zero plunge (Figs. 1 and 2). Understanding the source process of the 2007 Martinique earthquake and its exceptionally large NDC component is important because it has the potential to be a key end member of earthquake source complexity.

For this study, we applied potency density tensor inversion (PDTI; Shimizu *et al*. 2020) to teleseismic *P* waves generated by the 2007 Martinique earthquake. The PDTI method can estimate source processes including fault geometry by assuming a single plane (rather than multiple fault planes) but allowing arbitrary slip directions that are not necessarily parallel to that fault plane (Shimizu *et al.* 2020). It is therefore useful for modelling the source process of the 2007 Martinique earthquake, which is likely to have had multiple ruptures of different faulting styles.

METHOD

Seismic source processes can be estimated with conventional finite-fault inversions (e.g. Olson & Apsel 1982; Hartzell & Heaton 1983). However, these inversions constrain shear-slip directions to the direction perpendicular to the normal vector of the assumed fault planes, so we would need to assume an elaborate fault model for the 2007 Martinique earthquake, which is likely to have had multiple ruptures on different faults. Because of the few aftershocks (Fig. 2) and a lack of geodetic data, such an elaborate fault model would be difficult to envision. Application of the recently developed PDTI method to teleseismic *P* waves (Shimizu *et al.* 2020; Yamashita *et al.* 2021) allows estimation of the source processes of earthquakes with multiple ruptures on different faults with few

assumptions about fault geometry. The PDTI approach estimates the source process on an assumed fault plane represented by a spatio-temporal distribution of potency-rate density tensors (Ampuero & Dahlen 2005) that are calculated by superposition of five basis double-couple components (Kikuchi & Kanamori 1991) (Fig. 3). In this method, all directions of shear slip are permitted on the model fault plane (Shimizu *et al.* 2020). Therefore, PDTI can project multiple ruptures on different faults onto the model plane (e.g. Tadapansawut *et al*. 2022; Yamashita *et al*. 2022a).

The teleseismic *P* wave u_j observed at a station j is expressed in PDTI as

$$u_j(t) = \sum_{q=1}^{5} \int_S (G_{qj}(t,\xi) + \delta G_{qj}(t,\xi)) * \dot{D}_q(t,\xi)\, d\xi + e_{bj}(t), \qquad (2)$$

where G_{qj} is the calculated theoretical Green's function of the qth basis double-couple component, δG_{qj} is the modelling error on G_{qj} (Yagi & Fukahata 2011), $\dot{D}_q$ is the qth potency-rate density function, e_{bj} is background and instrumental Gaussian noise, ξ represents a position on the assumed model plane (S), and $*$ denotes the convolution operator in the time domain.

PDTI has a higher degree of freedom than conventional finite-fault inversions that may lead to unstable inversion and/or overfitting of the data. To avoid this problem, PDTI explicitly introduces an error term of the Green's function into the data covariance

matrix (Yagi & Fukahata 2011) and determines the relative weights of information from observed data and prior constraints using Akaike's Bayesian Information Criterion (Akaike 1980; Yabuki & Matsu'ura 1992; Sato *et al.* 2022).

Both synthetic tests and applications to real earthquakes have confirmed that PDTI projects stable and plausible spatio-temporal rupture distributions that include information about fault geometry onto the assumed model plane (e.g. Hicks *et al*. 2020; Okuwaki *et al*. 2020, 2021; Hu *et al*. 2021; Shimizu *et al*. 2021; Tadapansawut *et al*. 2021, 2022; Yamashita *et al*. 2021; Okuwaki & Fan 2022; Yamashita *et al*. 2022a; Yamashita *et al*. 2022b; Yagi *et al*. 2023).

We used the latest version of PDTI, which introduced time-adaptive smoothing constraints (Yamashita *et al*. 2022b) that can mitigate over-smoothing during a main rupture by dynamically changing smoothing strength to be inversely proportional to the amplitude of the potency-rate function (Yamashita *et al*. 2022b).

DATA AND MODELLING

We used teleseismic body *P* waves at epicentral distances of 30–100° obtained from the Data Management Center of the Incorporated Research Institutions for Seismology

(IRIS-DMC) for inputs to the PDTI. We chose waveforms recorded at 48 stations (Fig. 4a) where the signal-to-noise ratio was high and manually picked their first motions. Then, we converted the waveforms into velocity waveforms at a sample interval of 0.8 s. We used the velocity waveform data for 24 s after the picked initial time to mitigate the effect of reflected phases from structural discontinuities (e.g. the free surface) around the hypocentre. We assumed a 1-D velocity structure near the source, which we determined from the ak135 velocity model of Kennett *et al*. (1995) (Table S1) and then calculated the theoretical Green's function using the method of Kikuchi & Kanamori (1991). The uncertainty of the underground structure was accounted for by introducing the error term of the Green's function into the data covariance matrix (Yagi & Fukahata 2011).

We set the initial rupture point at 61.274°W, 14.944°N, and 156 km depth (USGS 2007). The pulse widths of the displacement teleseismic *P* waves tended to shorten as the azimuth approached south-southeast, indicating that the main rupture propagated to the south-southeast (Fig. 5). Thus, we assumed a horizontal 96 km × 78 km rectangular horizontal model plane striking 340°, which that would fit the rupture propagation to the south-southeast (Fig. 2). We discretized the model plane into source elements at 6 km intervals and then expanded the potency-rate density tensor function at each source element into a linear B-spline function with an interval of 0.8 s. The total

duration of the event was set at 20.8 s with a maximum rupture velocity of 4.5 km/s according to the shear wave velocity at the hypocentral depth indicated by the ak135 velocity model (Kennett *et al.* 1995) (Table S1).

RESULTS

The inverted source model for the 2007 Martinique earthquake explains the complexity of the observed waveforms (Figs 4b and S2). The total seismic moment of the best-fit double-couple solution, obtained by integrating the potency-rate density tensors in space and time, was 2.1×10^{20} N m (M_w 7.5). The NDC component accounts for 83% of the total moment tensor (Fig. 6). The P axis azimuth is 79° and it plunges at 44°. The T axis azimuth is 249° and it plunges at 45°. The moment-rate function, obtained by calculating the seismic moment-rate of the best-fit double-couple solution at each sampling time, shows a major peak of 3.0×10^{19} N m/s at 9.6 s after the origin time (Fig. 6).

The potency density distribution shows two main peaks (Fig. 6): one at the epicentre of the 2007 Martinique earthquake (northern peak) and another about 30 km southeast of the epicentre (southern peak). At the northern peak, the potency density tensor is almost entirely double-couple (6% NDC component). Its focal mechanism indicates a nearly vertical fault plane (84° dip) striking north with almost horizontal (10°

dip) nodal planes. The azimuth of the T axis around the northern peak (i.e. near the epicentre) ranges from 240° to 300° and plunges at 30–45° (Fig. 7). Because the azimuth and plunge of the T axis are consistent with those of the subducting slab (Fig. 2), we consider the focal mechanism at the northern peak to be down-dip extension (DDE). However, at the southern peak, the distribution of the potency density tensor indicates a 51% NDC component (Fig. 6). The azimuth of the T axis around the southern peak is concentrated at around 200° with plunge ranging from 0° to 30° (Fig. 7). The distributions of the P and B axes of the DDE mechanism are scattered over a wide range of azimuths, whereas the P, T and B axes of the strike-slip mechanism occupy narrow azimuthal ranges that are predominantly east–west, north–south and east–west, respectively (Fig. 7).

Sequential snapshots of the rupture evolution (Fig. S1) show multiple ruptures that we denote as sub-events E1, E2, E3, E4 and E5 (Fig. 8). Sub-event E1 propagated to the southeast with a strike-slip mechanism for 2 s after the origin time (hereafter, all times are relative to the origin time). Sub-event E2 started 25 km east of the epicentre with a DDE mechanism and propagated slowly eastward from 4 s to 10 s. Sub-event E3 started 30 km southeast of the epicentre with a DDE mechanism and propagated eastward from 5 s to about 10 s. Sub-event E4 started 20 km west of the epicentre with a DDE mechanism and propagated eastward from 8 s to about 14 s. Sub-event E5 started about 30 km

southeast of the epicentre with a strike-slip mechanism and propagated slowly to the southeast from 9 s to 16 s.

To evaluate the veracity of our source model, we re-ran the PDTI using an alternative velocity structure near the source (Table S2) that was based on the CRUST1.0 Global Model of Earth's Crust (Laske *et al.* 2013) otherwise using the same model settings and waveform data as in our original inversion. The focal mechanisms and rupture propagations of the five sub-events obtained in the original inversion can be identified given an alternative velocity structure (Fig. S3).

DISCUSSION

Our source model suggests that the 2007 Martinique earthquake included five sub-events (E1 to E5; Fig. 8). Although it is impossible to determine which of the two nodal planes of the focal mechanisms we obtained corresponds to the fault plane, it can be inferred by considering both the focal mechanisms and the distributions and directions of rupture.

For sub-event E1, the strike-slip rupture propagated south-eastwards, corresponding to a left-lateral strike-slip nodal plane striking northwest (Fig. 8). For sub-event E2, the DDE rupture propagated eastwards, which is orthogonal to the strike of the vertical nodal plane (Figs 8 and S1). The sub-event E2 rupture is therefore considered to

have propagated on a horizontal fault plane. Both the E3 and E4 sub-events had DDE mechanisms and propagated eastwards, indicating that these ruptures also propagated on a horizontal fault plane (Figs 8 and S1). The E5 sub-event had a strike-slip rupture that propagated to the south-southeast, corresponding to a left-lateral strike-slip nodal plane striking northwest (Fig. 8). These rupture directions and distributions suggest that the three sub-events with DDE mechanisms occurred on horizontal fault planes, whereas the two sub-events with strike-slip mechanisms occurred on left-lateral strike-slip fault planes.

Both of the sub-events with strike-slip mechanisms (E1 and E5) had left-lateral strike-slip fault planes striking northwest (Fig. 8), from which it can be inferred that they occurred on the same northwest-striking left-lateral strike-slip fault. Each of the three sub-events with DDE mechanisms (E2, E3 and E4) had horizontal fault planes, which suggests that these sub-events may also have occurred on one fault plane (Fig. 8). Thus, it is plausible that all of the five sub-events occurred on one of two fault planes. However, PDTI projects multiple fault ruptures onto a single model plane, so this is only one possible interpretation; it is possible that the sub-events occurred on five independent fault planes during the 2007 Martinique earthquake.

The rupture areas of sub-events E1 and E4 overlap near the epicentre of the 2007

Martinique earthquake (Figs 8 and S1). Overlapping rupture areas near the epicentre of the 2019 Peru intraslab earthquake have been attributed to re-rupture on a single fault (e.g. Hu *et al*. 2021; Vallée *et al*. 2023). Thus, the E4 sub-event may also have been a re-rupture of the fault of the E1 sub-event. However, our source model indicates that the E1 sub-event ruptured on a left-lateral strike-slip fault plane, whereas the E4 sub-event ruptured on a horizontal fault plane (Figs 8 and S1). Therefore, two ruptures near the hypocentre but at different times and on different fault planes is also plausible.

Our source model demonstrates that the focal mechanisms of the five sub-events of the 2007 Martinique earthquake were either strike-slip with a north–south T axis or DDE with an east–west T axis (Figs 6–8). In the area around the source region of the 2007 Martinique earthquake, the GCMT catalogue reports strike-slip earthquakes with north–south T axes, which is consistent with the strike-slip mechanism of our source model (Fig. 2). However, DDE earthquakes have not been identified in this region in the GCMT catalogue (Fig. 2), although they have been identified by ocean bottom seismometer observations (Lindner *et al.* 2022).

Our results show that the 2007 Martinique earthquake included two focal mechanisms (strike-slip and DDE) and that the NDC component of the total moment tensor was 83%, similar to the 90% NDC component given by the GCMT solution (Figs

2 and 6). In general, two conditions must be satisfied for the total moment tensor solution of an earthquake with two focal mechanisms to be a compensated linear vector dipole (i.e. to have a 100% NDC component; e.g. Frohlich *et al*. 1989). The first condition is that the two focal mechanisms must have parallel P axes (or T axes) and orthogonal the other two principal axes. The second condition is that the seismic moments of the ruptures of the two focal mechanisms must be equal (e.g. Frohlich *et al*. 1989) (Fig. 9). The NDC component increases progressively as these two conditions come to be satisfied.

The two focal mechanisms of our source model have nearly parallel P axes and nearly orthogonal T axes, thus almost satisfying the first condition (Fig. 7). Furthermore, the seismic moments of the DDE mechanism at the northern peak and the strike-slip mechanism at the southern peak are almost the same, therefore almost satisfying the second condition (Fig. 6). The unusually large NDC component (83%) observed during the 2007 Martinique earthquake likely reflects the near satisfaction of both conditions.

Earthquakes with large NDC components related to their inclusion of two or more sub-events with different focal mechanisms have been reported previously for intermediate-depth (70–300 km) and deep (>300 km depth) earthquakes (Kuge & Kawakatsu 1990, 1992, 1993; Kuge & Lay 1994). For example, Kuge & Kawakatsu (1990) analysed teleseismic body *P* waves generated by a deep earthquake and showed

that the inclusion of two sub-events with different mechanisms resulted in a large NDC component. However, there are very few examples of intermediate-depth earthquakes with large NDC components (other than the 2007 Martinique earthquake) for which complex source processes can be estimated. Our results show that PDTI, which can estimate complex source processes by assuming a model plane rather than a fault plane, can be used to clarify the seismic source process of intermediate-depth earthquakes for which low aftershock activity makes it difficult to recognize the complexity of the fault geometry.

Earthquakes that include multiple sub-events with similar focal mechanisms have been observed in oceanic intraplate earthquakes, for example, the 2012 Sumatra (M_W 8.6) and 2018 Gulf of Alaska (M_w 7.9) earthquakes (Duputel *et al.* 2012; Meng *et al.* 2012; Krabbenhoeft *et al.* 2018; Yamashita *et al.* 2021). The NDC components of the GCMT solutions for the 2012 Sumatra and 2018 Gulf of Alaska earthquakes are 22% and 47%, respectively, which seem to be small relative to the complexity of the source processes. There are also a few examples of earthquakes that include multiple sub-events with different focal mechanisms, for example the 2010 El Mayor-Cucapah (M_W 7.2) and 2016 Kaikoura (M_W 7.8) earthquakes, both of which occurred in complex fault zones (e.g. Wei *et al*. 2011; Fletcher *et al*. 2014; Hamling *et al*. 2017; Stirling *et al*. 2017; Litchfield

et al. 2018). However, the predominance of the moment tensor components corresponding to main ruptures of these two earthquakes resulted in relatively low (<60%) NDC components in their GCMT solutions (52% for the 2010 El Mayor-Cucapah and 32% for the 2016 Kaikoura earthquakes). Although the NDC component reflects the complexity of the seismic source process, the NDC component is not necessarily large in earthquakes with complex rupture processes. Given reliability of the NDC component across the different CMT catalogues has been an active research topic (e.g. Rösler *et al*. 2023), it is critical to estimate spatio-temporal distribution of potency-rate density tensors for our understanding of the complexity of ruptures in large earthquakes.

The 2007 Martinique earthquake is one of the largest recent earthquakes known to have a large NDC component. It is characterised by complex source processes, including both multiple sub-events and back-rupture propagation towards the epicentre. Several researchers have noted that slab dehydration may have elevated pore pressures in the source region (Bie *et al.* 2022; Ezenwaka *et al.* 2022; Hicks *et al.* 2023). It has also been recognised that reduced fault strength due to increased pore pressure can induce rupture on non-optimal fault planes, thus leading to diverse focal mechanism solutions (e.g. Terakawa *et al*. 2012). Furthermore, if fault strength is reduced, the likelihood of triggering multiple faults by stress changes during earthquakes would be expected to

increase. For the 2007 Martinique earthquake, the weakening of fault strength due to elevated pore fluid pressure associated with slab dehydration (e.g. Yamasaki & Seno 2003; Kita & Ferrand 2018) may have contributed to the generation of multiple sub-events with different focal mechanisms.

CONCLUSIONS

We applied PDTI to teleseismic *P* waves to model the complex seismic source processes of the 2007 Martinique earthquake, an intermediate depth intraslab earthquake in the Caribbean Sea. Our source modelling suggests that the earthquake incorporated five sub-events (E1 to E5) with two distinct mechanisms. Sub-events E1 and E5 had left-lateral strike-slip mechanisms on a northwest-striking fault plane, whereas sub-events E2, E3 and E4 had DDE mechanisms on an almost horizontal fault plane. The P axes of the strike-slip and DDE mechanisms were almost parallel, their T axes were almost orthogonal, and their seismic moments were almost equal. These characteristics approximate the conditions required for the 2007 Martinique earthquake to be considered to have had a large NDC component. The rupture of sub-event E4 featured back propagation (i.e. towards the epicentre) that crossed the rupture area of sub-event E1. The different focal mechanisms of sub-events E1 and E4, both of which were triggered near

the hypocentre, suggest they ruptured on different faults. The complex seismic source processes of the 2007 Martinique earthquake may be related to weakening of fault strength due to elevated pore fluid pressure associated with dehydration of the down going slab.

Our results show that the application of PDTI to earthquakes with large NDC components can provide stable estimates of complex seismic source processes along a single model plane and that PDTI can provide useful information about the sources of complex intermediate depth intraslab earthquakes for which fault geometry assumptions are difficult.

ACKNOWLEDGMENTS

This work was supported by KAKENHI Grant-in-Aid for Scientific Research (C) 22K03751 from the Japanese Ministry of Education, Culture, Sports, Science and Technology. The facilities of IRIS Data Services and IRIS Data Management Center were used to access the waveforms, related metadata and derived products used in this study. IRIS Data Services are funded through the Seismological Facilities for the Advancement of Geoscience (SAGE) Award of the National Science Foundation under Cooperative Support Agreement EAR-1851048. We used FPSPACK (Gasperini & Vannucii 2003) to

manage the focal mechanism data obtained in our inversions. The code for the potency density tensor inversion was developed by Yuji Yagi, Kosuke Shimizu and Shinji Yamashita. The figures were created using graphics software packages matplotlib (v3.5.2, https://doi.org/10.1109/MCSE.2007.55; Hunter 2007), pyrocko (v2022.6.10, https://doi.org/10.5880/GFZ.2.1.2017.001; Heimann *et al.* 2017), and Generic Mapping Tools (v6.4.0; Wessel *et al*. 2019).

Data availability

All seismic data were obtained from the IRIS Wilber 3 system (https://ds.iris.edu/wilber3/) or from IRIS Web Services (https://service.iris.edu/), including the following seismic networks: (1) the Canadian National Seismograph Network (CN; https://doi.org/10.7914/SN/CN); (2) GEOSCOPE (G; https://doi.org/10.18715/GEOSCOPE.G); (3) GEOFON (GE; https://doi.org/10.14470/TR560404); (4) the Global Telemetered Seismograph Network (USAF/USGS) (GTSN) (GT; https://doi.org/10.7914/SN/GT); (5) the IRIS/IDA Seismic Network (II; https://doi.org/10.7914/SN/II); (6) the Global Seismograph Network (IU; https://doi.org/10.7914/SN/IU); (7) the Mediterranean Very Broadband Seismographic Network (MN; https://doi.org/10.13127/SD/fBBBtDtd6q); and (8) the Netherlands

Seismic and Acoustic Network (NL; https://doi.org/10.21944/e970fd34-23b9-3411-b366-e4f72877d2c5). The CRUST 1.0 structural velocity model is available at https://igppweb.ucsd.edu/~gabi/crust1.html. Global Centroid Moment Tensor (GCMT) solutions are available at https://www.globalcmt.org/CMTsearch.html. The slab2 model is available at https://doi.org/10.5066/F7PV6JNV.

REFERENCES

Abercrombie, R.E., Antolik, M. & Ekström, G., 2003. The June 2000 7.9 earthquakes south of Sumatra: Deformation in the India-Australia Plate. *J. geophys. Res.: Solid Earth*, **108**, ESE 6-1-ESE 6-16. doi:10.1029/2001JB000674

Akaike, H., 1980. Likelihood and the Bayes procedure. *Trabajos de Estadistica Y de Investigacion Operativa*, **31**, 143–166. doi:10.1007/BF02888350

Ampuero, J.-P. & Dahlen, F.A., 2005. Ambiguity of the Moment Tensor. *Bull. seism. Soc. Am.*, **95**, 390–400. doi:10.1785/0120040103

Avouac, J.-P., Ayoub, F., Wei, S., Ampuero, J.-P., Meng, L., Leprince, S., Jolivet, R., *et al.*, 2014. The 2013, Mw 7.7 Balochistan earthquake, energetic strike-slip reactivation of a thrust fault. *Earth planet. Sci. Lett.*, **391**, 128–134. doi:10.1016/j.epsl.2014.01.036

Bie, L., Hicks, S., Rietbrock, A., Goes, S., Collier, J., Rychert, C., Harmon, N., *et al.*, 2022. Imaging slab-transported fluids and their deep dehydration from seismic velocity tomography in the Lesser Antilles subduction zone. *Earth planet. Sci. Lett.*, **586**. doi:10.1016/j.epsl.2022.117535

Bird, P., 2003. An updated digital model of plate boundaries. *Geochem. Geophys. Geosyst.*, **4**. doi:10.1029/2001GC000252

Cooper, G.F., Macpherson, C.G., Blundy, J.D., Maunder, B., Allen, R.W., Goes, S., Collier, J.S., *et al.*, 2020. Variable water input controls evolution of the Lesser Antilles volcanic arc. *Nature*, **582**, 525–529. doi:10.1038/s41586-020-2407-5

DeMets, C., Gordon, R.G. & Argus, D.F., 2010. Geologically current plate motions. *Geophys. J. Int.*, **181**, 1–80. doi:10.1111/j.1365-246X.2009.04491.x

Duputel, Z., Kanamori, H., Tsai, V.C., Rivera, L., Meng, L., Ampuero, J.P. & Stock, J.M., 2012. The 2012 Sumatra great earthquake sequence. *Earth planet. Sci. Lett.*, **351–352**, 247–257. doi:10.1016/j.epsl.2012.07.017

Dziewonski, A.M., Chou, T.A. & Woodhouse, J.H., 1981. Determination of earthquake source parameters from waveform data for studies of global and regional seismicity. *J. geophys. Res.*, **86**, 2825–2852. doi:10.1029/JB086iB04p02825

Ekström, G., Nettles, M. & Dziewoński, A.M., 2012. The global CMT project 2004–2010: Centroid-moment tensors for 13,017 earthquakes. *Phys. Earth planet. Inter.*, **200–201**, 1–9. doi:10.1016/j.pepi.2012.04.002

Ezenwaka, K., Marcaillou, B., Laigle, M., Klingelhoefer, F., Lebrun, J.F., Paulatto, M., Biari, Y., *et al.*, 2022. Thermally-constrained fluid circulation and seismicity in the Lesser Antilles subduction zone. *Earth planet. Sci. Lett.*, **597**. doi:10.1016/j.epsl.2022.117823

Fletcher, J.M., Teran, O.J., Rockwell, T.K., Oskin, M.E., Hudnut, K.W., Mueller, K.J., Spelz, R.M., *et al.*, 2014. Assembly of a large earthquake from a complex fault system: Surface rupture kinematics of the 4 April 2010 El Mayor-Cucapah (Mexico) Mw 7.2 earthquake. *Geosphere*, **10**, 797–827. doi:10.1130/GES00933.1

Frohlich, C., Riedesel, M.A. & Apperson, K.D., 1989. Note concerning possible mechanisms for non-double-couple earthquake sources. *Geophys. Res. Lett.*, **16**, 523–526. doi:10.1029/GL016i006p00523

Gasperini, P. & Vannucii, G., 2003. FPSPACK: a package of FORTRAN subroutines to manage earthquake focal mechanism data. *Comput. Geosci.*, **29**, 893–901. doi:10.1016/S0098-3004(03)00096-7

Hamling, I.J., Hreinsdóttir, S., Clark, K., Elliott, J., Liang, C., Fielding, E., Litchfield, N., *et al.*, 2017. Complex multifault rupture during the 2016 Mw 7.8 Kaikōura earthquake, New Zealand. *Science*, **356**. doi:10.1126/science.aam7194

Hartzell, S.H. & Heaton, T.H., 1983. Inversion of strong ground motion and teleseismic waveform data for the fault rupture history of the 1979 Imperial Valley, California, earthquake. *Bull. seism. Soc. Am.*, **73**, 1553–1583. doi:10.1785/BSSA07306A1553

Hayes, G.P., Moore, G.L., Portner, D.E., Hearne, M., Flamme, H., Furtney, M. & Smoczyk, G.M., 2018. Slab2, a comprehensive subduction zone geometry model.

Science, **362**, 58–61. doi:10.1126/science.aat4723

Heimann, S., Kriegerowski, M., Isken, M., Cesca, S., Daout, S., Grigoli, F., Juretzek, C., *et al.*, 2017. Pyrocko - An open-source seismology toolbox and library. GFZ Data Services. doi:10.5880/GFZ.2.1.2017.001

Hicks, S.P., Bie, L., Rychert, C.A., Harmon, N., Goes, S., Rietbrock, A., Wei, S.S., *et al.*, 2023. Slab to back-arc to arc: Fluid and melt pathways through the mantle wedge beneath the Lesser Antilles. *Sci. Adv.*, **9**. doi:10.1126/sciadv.add2143

Hicks, S.P., Okuwaki, R., Steinberg, A., Rychert, C.A., Harmon, N., Abercrombie, R.E., Bogiatzis, P., *et al.*, 2020. Back-propagating supershear rupture in the 2016 M w 7.1 Romanche transform fault earthquake. *Nat. Geosci.*, **13**, 647–653. doi:10.1038/s41561-020-0619-9

Hu, Y., Yagi, Y., Okuwaki, R. & Shimizu, K., 2021. Back-propagating rupture evolution within a curved slab during the 2019 Mw8.0 Peru intraslab earthquake. *Geophys. J. Int.*, **227**, 1602–1611. doi:10.1093/gji/ggab303

Hunter, J.D., 2007. Matplotlib: A 2D graphics environment. *Compt. Sci. Eng.*, **9**, 90–95. doi:10.1109/MCSE.2007.55

Kennett, B.L.N., Engdahl, E.R. & Buland, R., 1995. Constraints on seismic velocities in the Earth from traveltimes. *Geophys. J. Int.*, **122**, 108–124. doi:10.1111/j.1365-

246X.1995.tb03540.x

Kikuchi, M. & Kanamori, H., 1991. Inversion of complex body waves—III. *Bull. seism. Soc. Am.*, **81**, 2335–2350. doi:10.1785/BSSA0810062335

Kita, S. & Ferrand, T.P., 2018. Physical mechanisms of oceanic mantle earthquakes: Comparison of natural and experimental events. *Sci. Rep.*, **8**. doi:10.1038/s41598-018-35290-x

Knopoff, L. & Randall, M.J., 1970. The compensated linear-vector dipole: A possible mechanism for deep earthquakes. *J. geophys. Res.*, **75**, 4957–4963. doi:10.1029/JB075i026p04957

Krabbenhoeft, A., Huene, R. von, Miller, J.J., Lange, D. & Vera, F., 2018. Strike-slip 23 January 2018 MW 7.9 Gulf of Alaska rare intraplate earthquake: Complex rupture of a fracture zone system. *Sci. Rep.*, **8**. doi:10.1038/s41598-018-32071-4

Kuge, K. & Lay, T., 1994. Systematic non-double-couple components of earthquake mechanisms: the role of fault zone irregularity. *J. geophys. Res.*, **99**, 457–467. doi:10.1029/94jb00140

Kuge, Keiko & Kawakatsu, H., 1990. Analysis of A Deep "Non Double Couple" Earthquake Using Very Broadband Data. *Geophys. Res. Lett.*, **17**, 227–230. doi:10.1029/GL017i003p00227

Kuge, Keiko & Kawakatsu, H., 1992. Deep and intermediate-depth non-double couple earthquakes: interpretation of moment tensor inversions using various passbands of very broadband seismic data. *Geophys. J. Int.*, **111**, 589–606. doi:10.1111/j.1365-246X.1992.tb02114.x

Kuge, Keiko & Kawakatsu, H., 1993. Significance of non-double couple components of deep and intermediate-depth earthquakes: implications from moment tensor inversions of long-period seismic waves. *Phys. Earth planet. Inter.*, **75**, 243–266. doi:10.1016/0031-9201(93)90004-S

Laske, G., Masters, G., Ma, Z. & Pasyanos, M., 2013. Update on CRUST1.0 - A 1-degree Global Model of Earth's Crust. *Geophysical Research Abstracts*, **15**.

Lindner, M., Rietbrock, A., Bie, L., Goes, S., Collier, J., Rychert, C., Harmon, N., *et al.*, 2022. Bayesian regional moment tensor from ocean bottom seismograms recorded in the Lesser Antilles: Implications for regional stress field. *Geophys. J. Int.*. doi:10.1093/gji/ggac494

Litchfield, N.J., Villamor, P., Dissen, R.J. van, Nicol, A., Barnes, P.M., Barrell, D.J.A., Pettinga, J.R., *et al.*, 2018. Surface rupture of multiple crustal faults in the 2016 Mw 7.8 Kaikōura, New Zealand, earthquake. *Bull. seism. Soc. Am.*, **108**, 1496–1520. doi:10.1785/0120170300

Meng, L., Ampuero, J.-P., Stock, J., Duputel, Z., Luo, Y. & Tsai, V.C., 2012. Earthquake in a Maze: Compressional Rupture Branching During the 2012 M_w 8.6 Sumatra Earthquake. *Science*, **337**, 724–726. doi:10.1126/science.1224030

NASA JPL, 2013. NASA Shuttle Radar Topography Mission Global 1 arc second [Data set]. NASA EOSDIS Land Processes DAAC. doi:10.5067/MEaSUREs/SRTM/SRTMGL1.003

Okuwaki, R. & Fan, W., 2022, January 28. Oblique Convergence Causes Both Thrust and Strike-Slip Ruptures During the 2021 M 7.2 Haiti Earthquake. *Geophys. Res. Lett*. doi:10.1029/2021GL096373

Okuwaki, R., Hicks, S.P., Craig, T.J., Fan, W., Goes, S., Wright, T.J. & Yagi, Y., 2021, December 28. Illuminating a Contorted Slab With a Complex Intraslab Rupture Evolution During the 2021 Mw 7.3 East Cape, New Zealand Earthquake. *Geophys. Res. Lett*. doi:10.1029/2021GL095117

Okuwaki, R., Hirano, S., Yagi, Y. & Shimizu, K., 2020. Inchworm-like source evolution through a geometrically complex fault fueled persistent supershear rupture during the 2018 Palu Indonesia earthquake. *Earth planet. Sci. Lett.*, **547**. doi:10.1016/j.epsl.2020.116449

Olson, A.H. & Apsel, R.J., 1982. Finite faults and inverse theory with applications to the

1979 Imperial Valley earthquake. *Bull. seism. Soc. Am.*, **72**, 1969–2001. doi:10.1785/BSSA07206A1969

Rösler, B., Stein, S. & Spencer, B., 2023. When are Non-Double-Couple Components of Seismic Moment Tensors Reliable? *Seismica*, **2**. doi:10.26443/seismica.v2i1.241

Sato, D.S.K., Fukahata, Y. & Nozue, Y., 2022. Appropriate reduction of the posterior distribution in fully Bayesian inversions. *Geophys. J. Int*. doi:10.1093/gji/ggac231

Shimizu, K., Yagi, Y., Okuwaki, R. & Fukahata, Y., 2020. Development of an inversion method to extract information on fault geometry from teleseismic data. *Geophys. J. Int.*, **220**, 1055–1065. doi:10.1093/gji/ggz496

Shimizu, K., Yagi, Y., Okuwaki, R. & Fukahata, Y., 2021. Construction of fault geometry by finite-fault inversion of teleseismic data. *Geophys. J. Int.*, **224**. doi:10.1093/gji/ggaa501

Stirling, M.W., Litchfield, N.J., Villamor, P., Dissen, R.J. van, Nicol, A., Pettinga, J., Barnes, P., *et al.*, 2017. THE M W 7.8 2016 KAIKŌURA EARTHQUAKE: SURFACE FAULT RUPTURE AND SEISMIC HAZARD CONTEXT. *Bull. N.Z. Soc. Earthq. Eng.*, **50**, 73–84.

Sykes, L.R., McCann, W.R. & Kafka, A.L., 1982. Motion of Caribbean Plate during last

7 million years and implications for earlier Cenozoic movements. *J. geophys. Res.: Solid Earth,* **87**, 10656–10676. doi:10.1029/JB087iB13p10656

Tadapansawut, T., Okuwaki, R., Yagi, Y. & Yamashita, S., 2021. Rupture Process of the 2020 Caribbean Earthquake Along the Oriente Transform Fault, Involving Supershear Rupture and Geometric Complexity of Fault. *Geophys. Res. Lett.*, **48**. doi:10.1029/2020GL090899

Tadapansawut, T., Yagi, Y., Okuwaki, R., Yamashita, S. & Shimizu, K., 2022. Complex rupture process on the conjugate fault system of the 2014 Mw 6.2 Thailand earthquake. *Prog. Earth planet. Sci.*, **9**. doi:10.1186/s40645-022-00484-5

Terakawa, T., Miller, S.A. & Deichmann, N., 2012. High fluid pressure and triggered earthquakes in the enhanced geothermal system in Basel, Switzerland. *J. geophys. Res.: Solid Earth,* **117**. doi:10.1029/2011JB008980

Tozer, B., Sandwell, D.T., Smith, W.H.F., Olson, C., Beale, J.R. & Wessel, P., 2019. Global Bathymetry and Topography at 15 Arc Sec: SRTM15+. *Earth Space Sci.*, **6**, 1847–1864. doi:10.1029/2019EA000658

USGS, 2007. M 7.4 - 18 km WNW of Basse-Pointe, Martinique. Retrieved August 19, 2022, from https://earthquake.usgs.gov/earthquakes/eventpage/usp000ftj1/executive

Vallée, M., Xie, Y., Grandin, R., Villegas-Lanza, J.C., Nocquet, J.M., Vaca, S., Meng, L., *et al.*, 2023. Self-reactivated rupture during the 2019 Mw = 8 northern Peru intraslab earthquake. *Earth planet. Sci. Lett.*, **601**. doi:10.1016/j.epsl.2022.117886

Wei, S., Fielding, E., Leprince, S., Sladen, A., Avouac, J.P., Helmberger, D., Hauksson, E., *et al.*, 2011. Superficial simplicity of the 2010 El Mayorg-Cucapah earthquake of Baja California in Mexico. *Nat. Geosci.*, **4**, 615–618. doi:10.1038/ngeo1213

Wessel, P., Luis, J.F., Uieda, L., Scharroo, R., Wobbe, F., Smith, W.H.F. & Tian, D., 2019. The Generic Mapping Tools Version 6. *Geochem. Geophys. Geosyst.*, **20**, 5556–5564. doi:10.1029/2019GC008515

Xu, W., Feng, G., Meng, L., Zhang, A., Ampuero, J.P., Bürgmann, R. & Fang, L., 2018. Transpressional Rupture Cascade of the 2016 M_w 7.8 Kaikoura Earthquake, New Zealand. *J. geophys. Res.: Solid Earth*, **123**, 2396–2409. doi:10.1002/2017JB015168

Yabuki, T. & Matsu'ura, M., 1992. Geodetic data inversion using a Bayesian information criterion for spatial distribution of fault slip. *Geophys. J. Int.*, **109**, 363–375. doi:10.1111/j.1365-246X.1992.tb00102.x

Yagi, Y. & Fukahata, Y., 2011. Introduction of uncertainty of Green's function into waveform inversion for seismic source processes. *Geophys. J. Int.*, **186**, 711–720.

doi:10.1111/j.1365-246X.2011.05043.x

Yagi, Y., Okuwaki, R., Enescu, B. & Lu, J., 2023. Irregular rupture process of the 2022 Taitung, Taiwan, earthquake sequence. *Sci. Rep.*, **13**. doi:10.1038/s41598-023-27384-y

Yamasaki, T. & Seno, T., 2003. Double seismic zone and dehydration embrittlement of the subducting slab. *J. geophys. Res.: Solid Earth*, 108. doi:10.1029/2002jb001918

Yamashita, S., Yagi, Y. & Okuwaki, R., 2022a. Irregular rupture propagation and geometric fault complexities during the 2010 Mw 7.2 El Mayor-Cucapah earthquake. *Sci. Rep.*, **12**, 4575. doi:10.1038/s41598-022-08671-6

Yamashita, S., Yagi, Y., Okuwaki, R., Shimizu, K., Agata, R. & Fukahata, Y., 2021. Consecutive ruptures on a complex conjugate fault system during the 2018 Gulf of Alaska earthquake. *Sci. Rep.*, **11**, 5979. doi:10.1038/s41598-021-85522-w

Yamashita, S., Yagi, Y., Okuwaki, R., Shimizu, K., Agata, R. & Fukahata, Y., 2022b. Potency density tensor inversion of complex body waveforms with time-adaptive smoothing constraint. *Geophys. J. Int.*, **231**, 91–107. doi:10.1093/gji/ggac181

Yue, H., Lay, T. & Koper, K.D., 2012. En échelon and orthogonal fault ruptures of the 11 April 2012 great intraplate earthquakes. *Nature*, **490**, 245–249. doi:10.1038/nature11492

Supporting information

Tables S1 and S2. Velocity structure models used for calculating the Green's function.

Figure S1. Full snapshots of the potency-rate density tensors

Figure S2. Waveform fitting between observed and synthesized waveforms.

Figure S3. Summary of result of the sensitivity test using 1-D velocity structure near the source based on CRUST1.0.

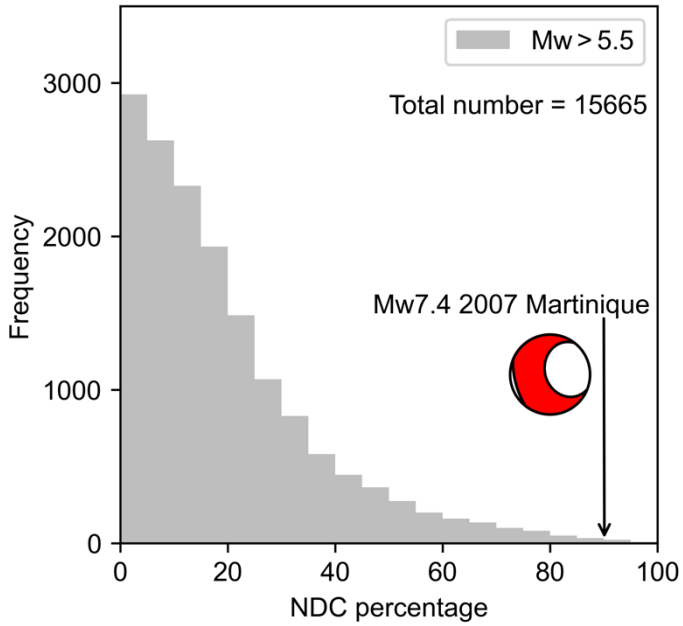

Figure 1. Frequency distribution of non-double-couple (NDC) of GCMT solutions for events of $M_w > 5.5$ recorded between 1 Jan 1976 and 1 Feb 2023 (Dziewonski *et al.* 1981; Ekström *et al.* 2012). The histogram bin width is 5% and the red beach ball shows the GCMT solution for the 2007 M_w 7.4 Martinique earthquake, which had a 90% NDC component.

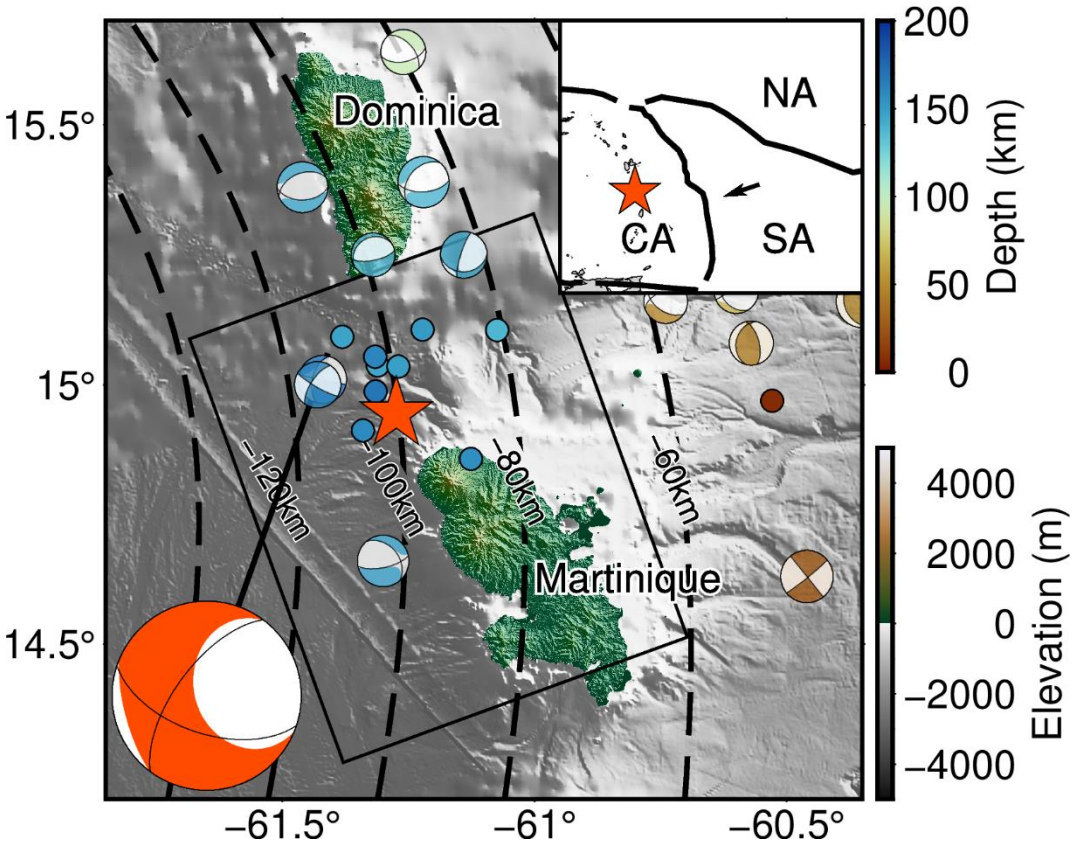

Figure 2. Seismotectonic summary of the region of the 2007 Martinique earthquake. The orange beach ball is the GCMT solution (Dziewonski *et al.* 1981; Ekström *et al.* 2012) of the 2007 main shock (epicentre marked by the orange star; USGS 2007). The other beach balls are GCMT solutions for earthquakes (other than the main shock) in the same region between 1 Jan 1976 and 1 Feb 2023. The coloured circles are the epicentres of aftershocks of the 2007 earthquake that were reported by USGS during the month following the main shock. The blue and brown beach balls and circles are coloured according to depth. The dashed lines are contours of slab depth (Hayes *et al.* 2018). Background topography is

from the SRTMGL1 data set (NASA JPL 2013) and background bathymetry is from the SRTM15+V2 data set (Tozer *et al.* 2019). The black rectangle represents the assumed model plane. In the inset regional map, the black lines represent plate boundaries (Bird 2003) and the arrow shows the direction of motion of the South America plate relative to the fixed Caribbean plate according to MORVEL 2010 plate velocity estimates (DeMets *et al.* 2010). NA, North America plate; SA, South America plate; CA, Caribbean plate.

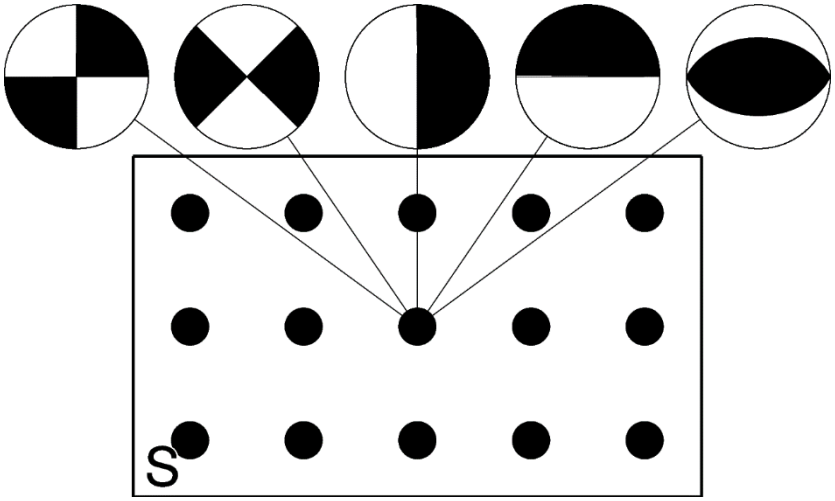

Figure 3. Schematic representation of potency density tensors at each source node on the model plane *S* in PDTI. The beach balls denote five basis double-couple components that are not rotated according to the model plane geometry (Kikuchi & Kanamori 1991).

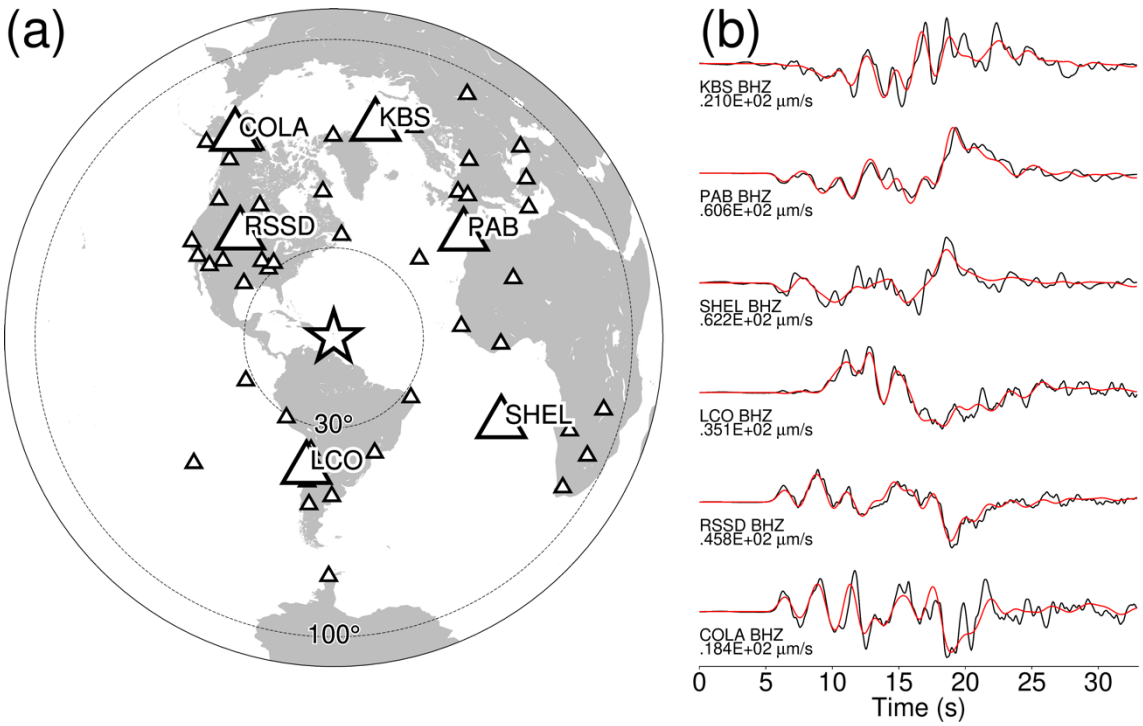

Figure 4. Distribution of teleseismic stations and waveform fitting. (a) Azimuthal equidistant projection of the stations used in the inversion. The star marks the epicentre of the 2007 Martinique earthquake (USGS 2007) and the triangles show the station locations. The inner and outer circles mark epicentral distances of 30° and 100°, respectively. (b) Six examples (large triangles in panel a) of fitting synthetic waveforms (red traces) to observed waveforms (black traces).

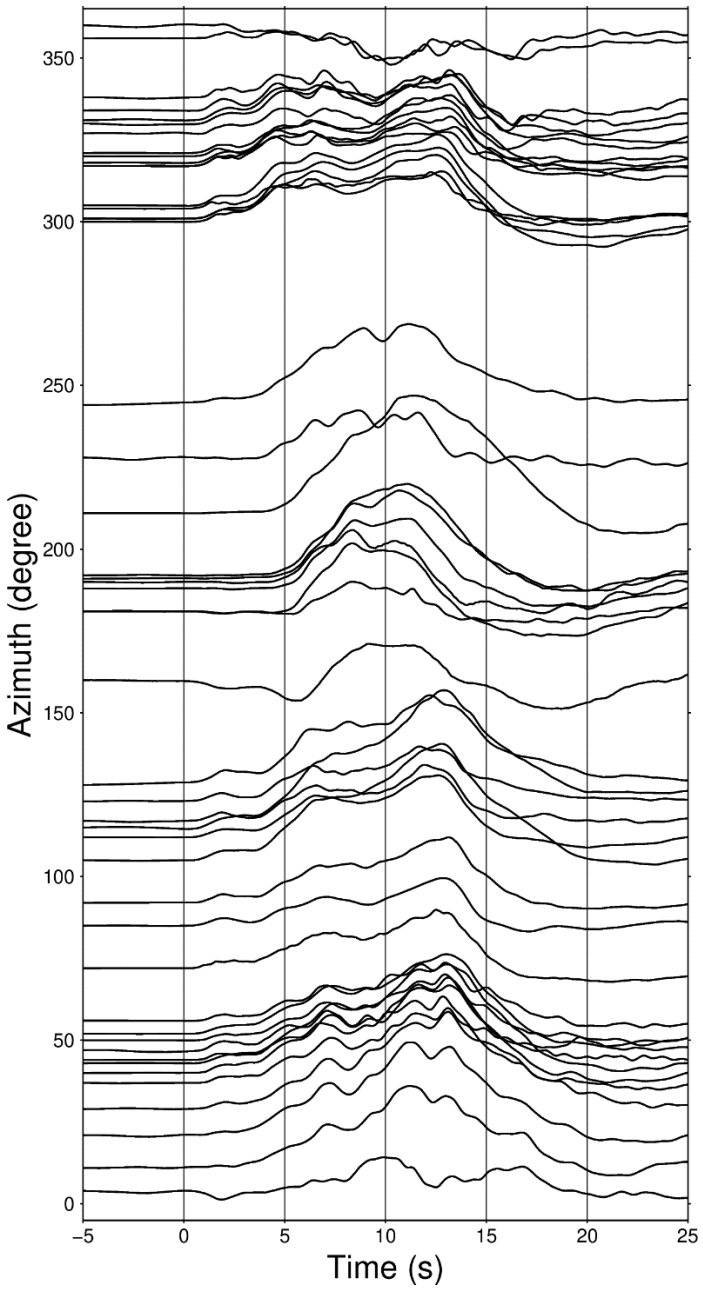

Figure 5. Displacement waveforms observed at the 48 stations shown in Figure 4a. The vertical axis is the azimuth of the station from the main shock. The horizontal axis is time elapsed since the *P* wave first motion. Note the polarity reversal of the observed waveforms at stations at less than 140° azimuth from the main shock.

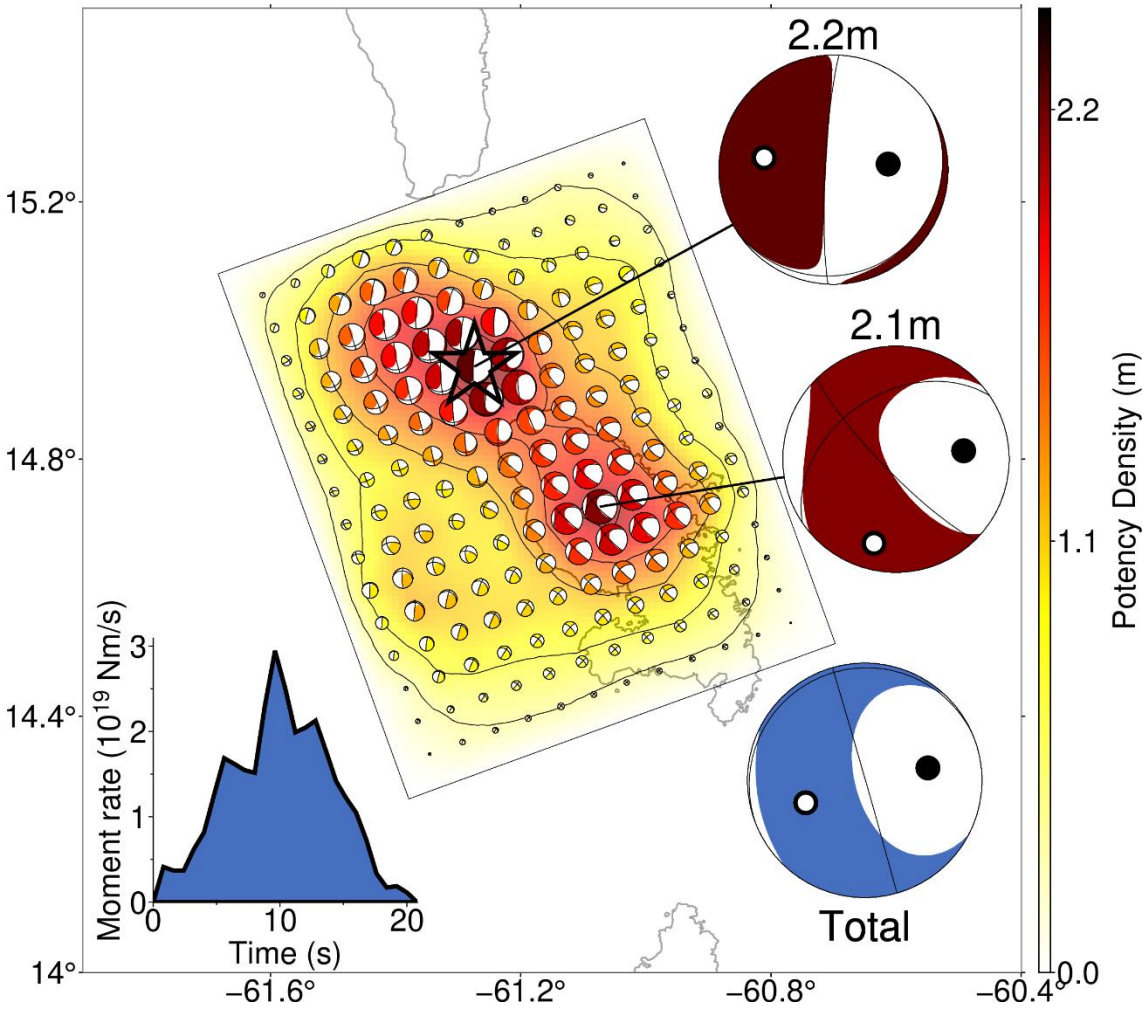

Figure 6. Summary of inversion results. Beach balls denote potency density tensors. Beach balls are coloured and scaled by potency density. The uppermost and middle large beach balls show the potency density tensors at the northern (2.2 m) and southern (2.1 m) peaks of potency density, respectively. The large blue (lowermost) beach ball represents the total moment tensor. Black and white circles within the large beach balls denote the P and T axes, respectively. The star denotes the epicentre of the 2007 Martinique

earthquake (USGS 2007). The left bottom inset panel shows the moment-rate time function.

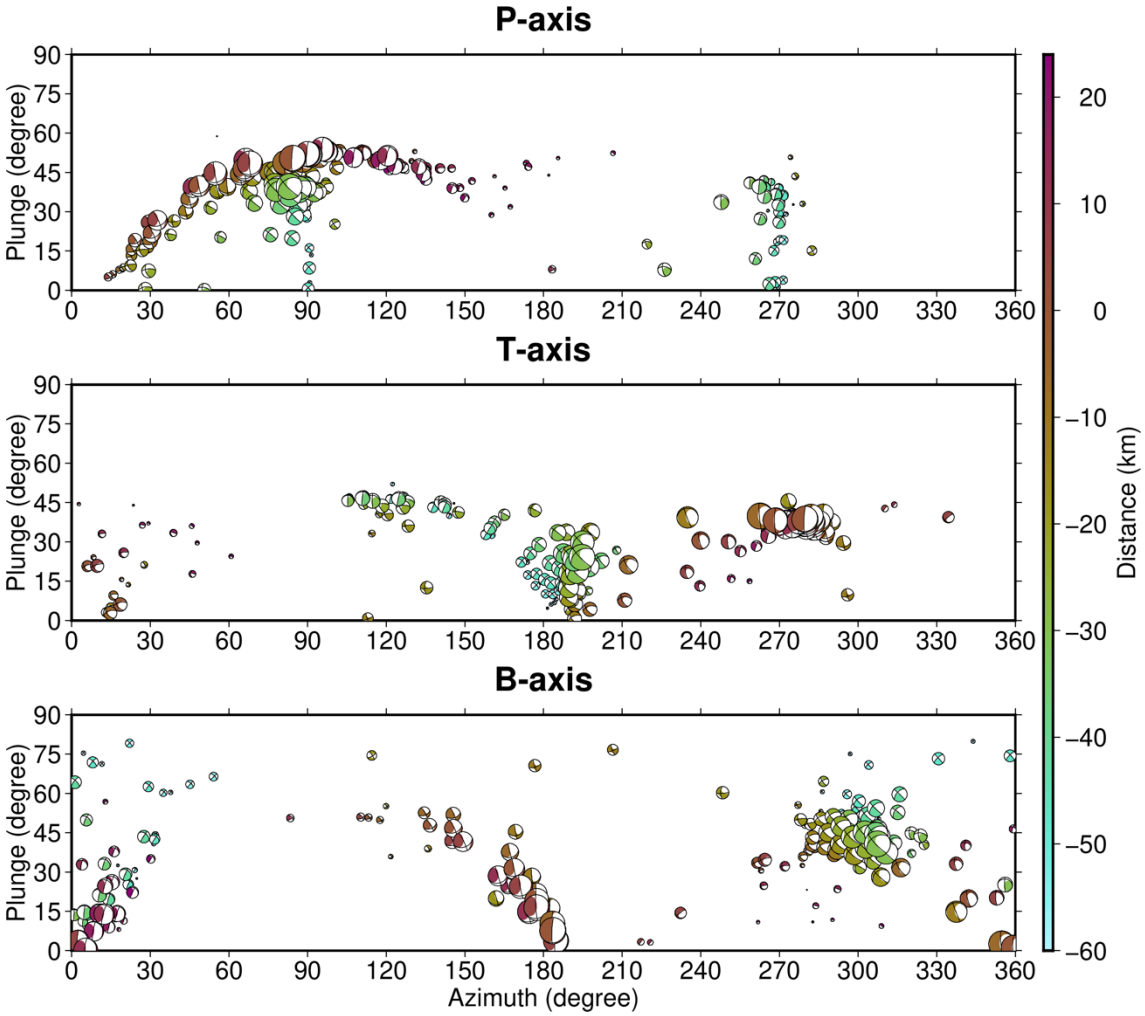

Figure 7. Azimuth versus plunge of the P, T and B axes of potency density tensors. The beach balls are scaled by potency density and coloured by distance from the epicentre along the northwest strike of the assumed model plane. Positive and negative distances represent locations northwest and southeast of the epicentre, respectively.

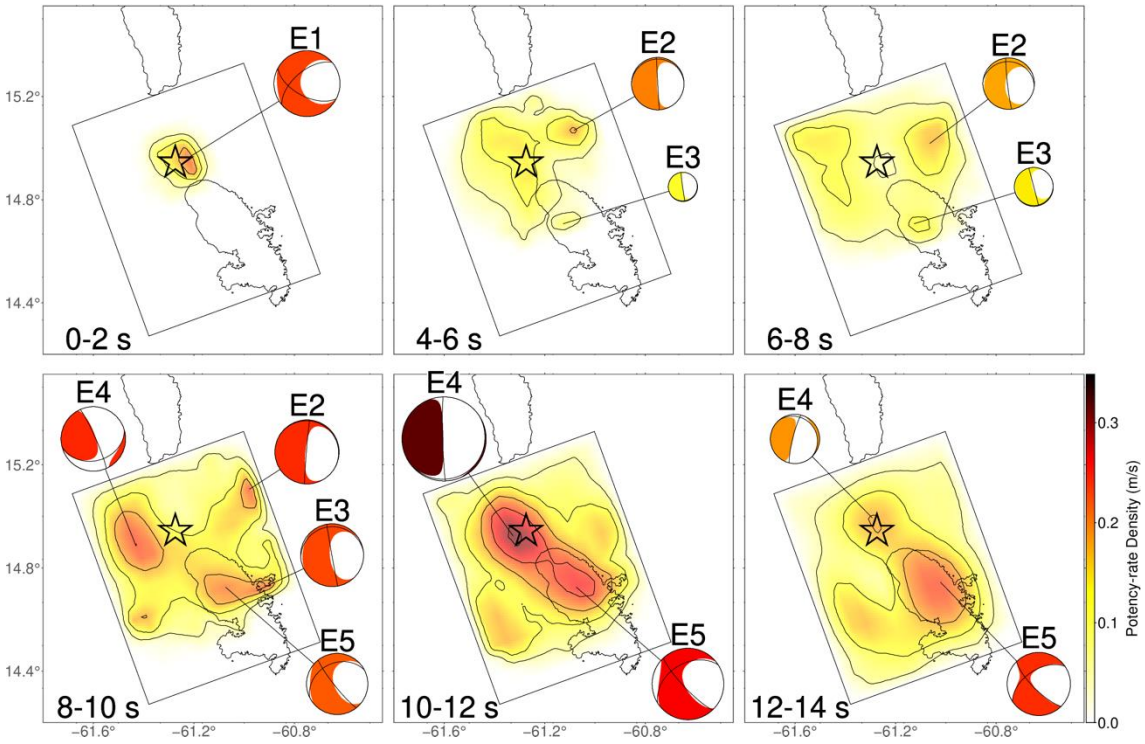

Figure 8. Selected snapshots of the potency-rate density tensors showing beach balls for the highest potency-rate densities for each of five sub-events (E1–E5). The beach balls are coloured and scaled by potency-rate density. The star denotes the epicentre of the 2007 Martinique earthquake (USGS 2007).

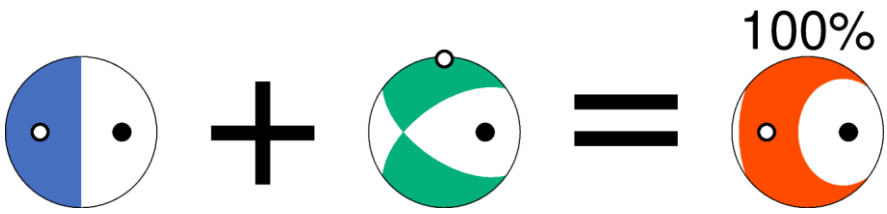

Figure 9. An example that demonstrates how the sum of two focal mechanisms is a compensated linear vector dipole moment tensor. The left (blue) and middle (green) focal mechanisms are two input focal mechanisms. The strike, dip and rake of one of the nodal planes of the blue focal mechanism are 0°, 0° and –90°, respectively. The blue focal mechanism has a P axis azimuth of 90° and a dip of 45°, a T axis azimuth of 270° and a dip of 45°, and a B axis azimuth of 0° and a dip of 0°. The strike, dip and rake of one of the nodal planes of the green focal mechanism are 125°, 60° and –35°, respectively. The green focal mechanism has a P axis azimuth of 90° and a dip of 45°, a T axis azimuth of 0° and a dip of 0°, and a B axis azimuth of 270° and a dip of 45°. The right (red) focal mechanism (the sum of the blue and green focal mechanisms) is entirely (100%) a non-double-couple mechanism. For each of the three focal mechanisms, the black and white circles denote the P and T axes, respectively.